Original Research

Effect of Cobalt Substitution on the Microstructure of Copper–Zinc Ferrite Nanostructures: A Study Using Williamson–Hall Models

Mariam O. Abd Alkareem [1], Tagreed M. Al-Saadi [2*], Anaam W. Watan [2]

[1] Department of Physics, College of Education, Mustansiriya University, Baghdad, Iraq;
[2] College of Education for Pure Science, Ibn Al Haitham, University of Baghdad, Baghdad, Iraq.
* Correspondence: taghreed.m.m@ihcoedu.uobaghdad.edu.iq

Received: March 10, 2026; Accepted: June 1, 2026

Abstract: In this research, $Co_xCu_{0.2}Zn_{0.8-x}Fe_2O_4$ nanoferrites (x = 0.0, 0.03, 0.06, 0.09, and 0.12) were prepared through the sol–gel method, and the effects of cobalt substitution on their structural and microscopic properties were investigated. X-ray diffraction (XRD) results revealed the formation of a pure cubic spinel phase without secondary phases, with the lattice constant gradually decreasing as the cobalt concentration increased. Crystal size, strain, and stress were analyzed by employing the Scherrer equation and three Williamson–Hall model models (uniform deformation, uniform stress, and uniform deformation energy density models). Results showed that extracted values varied depending on the model used because the models had different physical assumptions related to the strain and stress within the crystal lattice. Field-emission scanning electron microscopy (FESEM) images revealed partial agglomeration, nonuniform grain distribution, and grain sizes ranging from 65 ± 5 nm to 83 ± 10 nm. The crystal size inferred from XRD clearly differed from the grain size inferred from FESEM, confirming the polycrystalline nature of the prepared samples. The results of this study indicate that cobalt substitution directly affects the structural and microscopic properties of the prepared system.

Keywords: nanoferrites, cobalt substitution, sol–gel method, Williamson–Hall, lattice strain

1. Introduction

Nanoferrites with the generic formula of MFe_2O_4, where M indicates a divalent ion, namely, Co^{2+}, Zn^{2+}, or Cu^{2+}, have been the subject of great interest in recent decades because of their numerous structural, magnetic, and electrical properties. These oxides possess a cubic spinel-type structure in which the divalent cation and iron ions exist in tetravalent (A) and octavalent (B) positions and therefore exhibit diverse physical properties [1]. Given their excellent chemical stability and tunable magnetism, they are ideal candidates for various applications, including catalysts, sensors, magnetic recording media, and biomedicine [2]. Among nanoferrites, mixed ferrites with cobalt, copper, and zinc ions are a special class of materials with structural and physical properties that can be tailored in response to cationic substitution. Cation substitution at specific sites of the crystal lattice causes volume changes, lattice stresses, and internal stress distribution, thereby influencing electrical conductance, magnetic anisotropy, and mechanical stability [3]. Among the various elements used as substituents, cobalt has attracted considerable attention because Co2+ not only leads to the improvement of magnetic interactions but also affects the distribution of cations between the A and B sites [4]. Sol–gel synthesis is a method for the fabrication of nanoferrites with a high degree of purity. It exhibits simplicity and enables the easy control of chemical composition and crystal size. This route is based on the conversion of the starting solution of

metal salts into a colloidal solution (sol) that condenses into a homogeneous gel at a molecular level, thereby resulting in the uniform distribution of spinel-forming ions [5]. It has low calcining requirements for crystallization and generates highly homogeneous, regularly sized nanopowders. It enhances structural and magnetic properties, making ferrites prepared in this manner suitable for advanced technological applications [6]. X-ray diffraction (XRD) is among the most common methods used to investigate the crystal structure and microscopic stress of nanoferrites [7]. References on the use of the Scherrer equation, which considers internal stress, to predict crystallite size on the basis of diffraction peak broadening do not exist. Williamson–Hall (W–H) models, wherein the contributions of crystallite size and stress to peak broadening are separated, are therefore important [8]. Developed models, such as the uniform deformation model (UDM), uniform stress model (USDM), and uniform deformation energy density model (UDEDM), have various capabilities for understanding the mechanical and structural characteristics of nanoferrites [9].

This study involves the synthesis of $Co_xCu_{0.2}Zn_{0.8-x}Fe_2O_4$ nanoferrites through the spontaneous combustion sol–gel approach and the characterization of structural properties by using XRD measurements. The effects of cobalt substitution on crystal lattice parameters, crystal size, internal stresses, and deformation energy density are also studied. The underlying analytical formulas connecting chemical content with structural properties and determining the best cobalt content for increased stability and improved practical application potential could be clarified through the adoption of existing methods and developed analytical models.

2. Materials and methods

High-purity zinc nitrate hexahydrate ($Zn[NO_3]_2{\cdot}6H_2O$), copper nitrate trihydrate ($Cu[NO_3]_2{\cdot}3H_2O$) (Aldrich), cobaltous nitrate hexahydrate ($Co[NO_3]_2{\cdot}6\ H_2O$), Aldrich), and iron (III) nitrate nonahydrate ($Fe[NO_3]_3{\cdot}9H_2O$) were used as metal ion precursors. Citric acid ($C_6H_8O_7$) was employed as a complexing agent, ammonium hydroxide (NH_4OH) solution was utilized for pH adjustment, and distilled water was used as the reaction medium. Glass beakers, a magnetic hot plate, a digital pH meter, and an electric furnace were utilized in material preparation. The characterization facilities employed an XRD analyzer to determine crystalline structure.

$Co_xCu_{0.2}Zn_{0.8-x}Fe_2O_4$ (where x = 0, 0.03, 0.06, 0.09, and 0.12) nanoferrites were prepared as follows: Copper or cobalt additives were used to synthesize cobalt-substituted zinc ferrite nanoparticles. The required molar ratios of zinc nitrate, copper nitrate, cobalt nitrate, and ferric nitrate were precisely computed on the basis of chemical formulas and dissolved in 50 ml of deionized water under magnetic stirring. A citric acid complexing agent was added to the metal ions (dissolved in 50 ml of deionized water) in a 1:1 molar ratio and then stirred continuously. The solution pH was neutralized to 7 with ammonium hydroxide solution, and a color change was observed as a function of pH. The mixture was then heated under rigorous stirring at 80 °C–90 °C to form a gel. The resulting gel was subsequently dried at 120 °C for 12 h in a drying oven to obtain the precursor powder. The powder was calcined at 600 °C for 4 h in an electric furnace to form the final ferrite crystal structure, as shown in Figure 1. The crystalline nature of the prepared compounds was studied through XRD. Diffractograms were obtained in the 2θ range of 10°–80°, with a wavelength (λ) of Cu-Kα radiation of 1.5406 Å. Match! software (Crystal Impact Contact Page, Bonn, Germany) was utilized to analyze the results, and the effects of ferrite structure and cobalt concentration on crystalline parameters were compared with standard data (JCPDS).

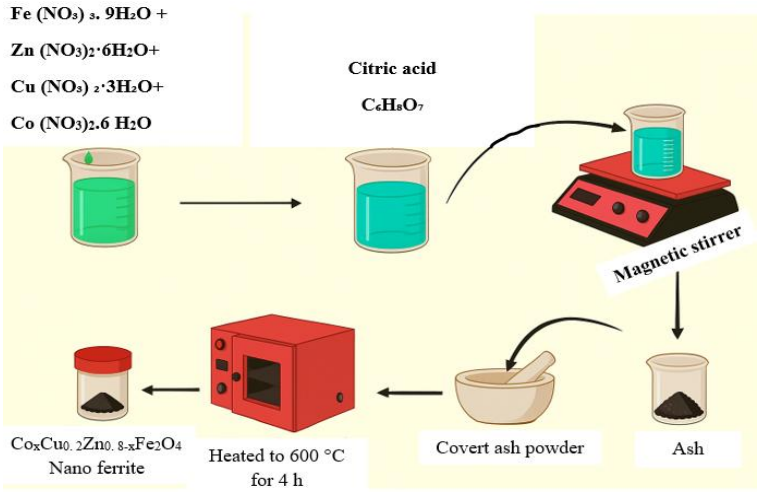

Figure 1. Sol–gel method for the preparation of $Co_xCu_{0.2}Zn_{0.8-x}Fe_2O_4$ nanoferrites.

3. Results and discussion

Figure 2 provides the diffraction patterns of $Co_xCu_{0.2}Zn_{0.8-x}Fe_2O_4$ nanospinels with x = 0, 0.03, 0.06, 0.09, and 0.12. Characteristic peaks are observed at the (220), (311), (400), (511), and (440) planes [10], with the (311) peak showing the maximum intensity. The peak distribution is consistent with the cubic spinel structure (space group Fd-3m) and supports the high phase purity of the powder samples (no distinct secondary peaks related to the individual cobalt, zinc, and copper oxides or the magnetite and hematite phases are observed). A slight shift in the peak locations toward large 2θ values is expected with increasing cobalt substitution (high x), implying a contraction in the lattice constant because of differences in ionic radii and a preference for crystalline sites [11]. The lattice constant can be estimated for each sample by calculating the interatomic distance d from the Bragg equation then using the relationship $a = d\sqrt{(h^2 + k^2 + l^2)}$ for each characteristic reflection and subsequently taking the weighted average of the strong reflections [12,13].

The peak width (full width at half maximum [FWHM]) contains information on crystal size and microscopic stresses. A width that decreases with increasing x indicates enhanced crystallization and crystal growth (high D), whereas an increase in width indicates small crystals and/or increased stresses resulting from cationic heterogeneity and lattice defects. The change in peak intensity ratios, particularly the ratios of the (220), (400), and (440) peaks to the (311) peak, could reflect a cationic redistribution between the A and B sites in the spinel structure [14]. Zn^{2+} tends to prefer the A site (with the spinel close to normal), Co^{2+} prefers the B site (with the spinel tending toward inversion), and Cu^{+2} may occupy either site depending on preparation conditions [15]. From a functional perspective, the expected lattice shrinkage or improved crystallinity with the introduction of cuprates could lead to a slight increase in magnetic anisotropy and improved grain structural consistency. The nanoscale crystal sizes also indicate that grain boundaries and stresses play a clear role in determining the final properties [16].

The acquired XRD patterns were examined by utilizing Match! Software (Crystal Impact Contact Page, Bonn, Germany) for phase identification and comparison with standard (JCPDS) data, as presented in Table 1, whereas the theoretical density of ferrite was evaluated via XRD by employing the relation [17].

$$\rho = \frac{N.M_W}{N_A.V} \qquad (1)$$

where V is the volume of the unit cell, N indicates the number of atoms within the unit cell, N_A is Avogadro's number, and M_w specifies the molar mass. The distances between magnetic ions (hopping length) at sites A and B were measured by using the following formulas [18]:

$$L_A = \frac{a\sqrt{3}}{4}, \quad (2)$$

$$L_B = \frac{a\sqrt{2}}{4}. \quad (3)$$

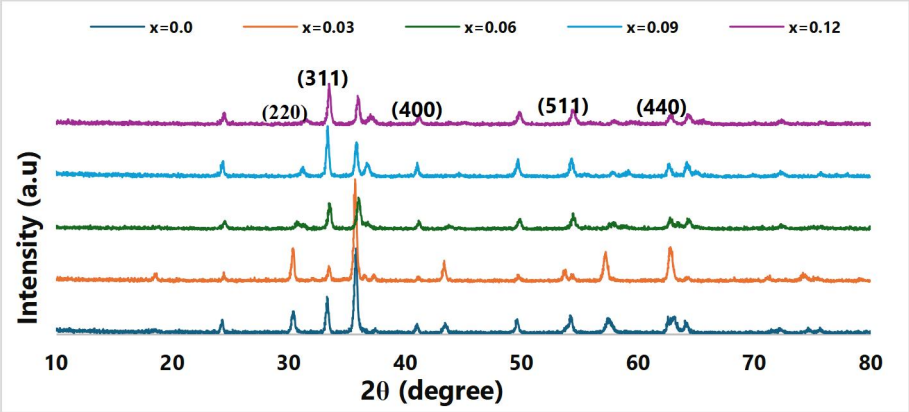

Figure 2. XRD spectra of $Co_xCu_{0.2}Zn_{0.8-x}Fe_2O_4$ nanoferrites.

Table 1. Lattice constants, densities, and hopping lengths of $Co_xCu_{0.2}Zn_{0.8-x}Fe_2O_4$ nanoferrites.

x	(g/cm^3)	a(Å)	L_A (Å)	L_B (Å)
0.00	5.524	8.339	3.611	2.948
0.03	5.414	8.395	3.635	2.968
0.06	5.637	8.280	3.585	2.927
0.09	5.682	8.260	3.577	2.920
0.12	5.884	8.179	3.542	2.892

The structural and density parameters derived from XRD are presented in Table 1. These parameters consistently fluctuate with cobalt content ($0 \le x \le 0.12$). These fluctuations illustrate the crucial effect of chemical composition on the basic structural features of the nanoferrites and the role of ionic substitutions in the spinel lattice. The lattice parameter (a) systematically decreases with increasing cobalt content [19]. It decreases stage by stage from 8.339 Å at x = 0.00 to 8.179 Å at x = 0.12. The close ionic radii of Zn^{2+} and Co^{2+} suggest that ionic size differences cannot be the exclusive cause of the observed lattice shrinkage. Rather, cation redistribution, altered bonding properties, and increased interionic interactions within the spinel structure are more likely than ionic size differences to be responsible for lattice shrinkage [20]. Moreover, increasing cobalt content may affect the spatial distribution of different ions (e.g., Cu^{2+} and Fe^{3+}) in A and B sites, both of which participate in the rearrangement and general contraction of the crystalline lattice.

Density varies nonlinearly with x: it first decreases from 5.524 g/cm^3 to 5.414 g/cm^3 (for x = 0.03) then quickly reaches 5.884 g/cm^3 (x = 0.12). This intricate behavior is associated with mass and volume effects [21]. The first decrease can be explained by the increase in crystal unit size at x = 0.03 (this parameter can increase to 8.395 Å), whereas density increases again with the increase in x value (because of the dominance of lattice shrinkage and increase in molar mass after the substitution of zinc [atomic mass of 65.38 g/mol] with cobalt [atomic mass of 58.93 g/mol]). The final increase in density at the highest cobalt content is attributed not only to mass gain but also to the volume contraction of the unit cell [20].

Similar to the lattice constant, the bond lengths at the A (L_A) and B (L_B) sites contract. The concurrent decrease in L_A and L_B indicates that substitution influences A and B sites, corroborating the phenomenon of cation redistribution within the spinel lattice. This behavior aligns with previously documented ion

rearrangement processes [22]. This small shift in ionic bonds indicates charge reordering and an electrostatic balance in the crystal lattice that are essential for the electrical and magnetic performance of the nanoferrites [23]. These compositional changes can be rationalized by a complex ionic substitution mechanism in which Co^{2+} replaces Zn^{2+} at A sites and Cu^{+2} partially redistributes between A and B sites to balance charge. This phenomenon results in inhomogeneous lattice stress and variations in the energies of ionic interactions, changes that are apparent in the lattice constant and bond distances [24]. Lattice shrinkage and ion redistribution reveal large A–B site exchange interactions that could lead to improvements in magnetic properties, such as Curie temperature and magnetic susceptibility. Moreover, the variation in bond length affects the electron bandwidth and conductivity of the materials, making this set of materials good candidates for studies on the synergetic relationship between structural and magnetic properties [25].

The Scherrer equation is an equation used in materials science to infer the average size of crystallites in a solid from the broadening of a diffraction peak in a powder diffractometer spectrum. This equation is based on the concept that XRD peaks widen as a result of small crystals, with small crystals intensifying this effect. The general expression of the Scherrer equation is [26, 27]

$$D = \frac{K\lambda}{\beta Cos\theta} \qquad (4)$$

where D is the crystallite size (in nm or Å), K is the shape factor (K ≈ 0.9), λ is the wavelength of X-rays (nm or Å), β is the FWHM in radians corrected for instrument broadening, and θ is the Bragg angle.

The above equation is an oversimplified and accurate but approximate relation providing the crystallite size but not the true size of particles given that one particle may typically have numerous subcrystals. It also disregards the influence of particle strain. Instrumental broadening must be performed to calculate the strain and size effect [28]. The corrected instrumental broadening β_{hkl} can be evaluated by utilizing the expression [29].

$$\beta^2 = [(\beta^2_{\text{measured}}) - (\beta^2_{\text{instrumental}})]^{1/2}. \qquad (5)$$

The result of applying the Scherrer equation is provided in Table 2.

The W–H method is an analytical technique used on XRD data to distinguish between the contributions of small crystal sizes and microstrain stresses to the broadening of diffraction peaks. While the Scherrer equation provides an estimate of crystal size only, the W–H method allows the separation of the effects of size and stress from peak width.

In the UDM, the deformation (stress) in the crystal is assumed to be uniformly distributed in all directions. The basic formula for this model is [30,31].

$$\beta \cos\theta = \frac{K\lambda}{D} + 4\varepsilon \sin\theta. \qquad (6)$$

The UDM is simple and suitable for isotropic materials. However, complex models, such as the UDSM or UDEDM, may be required for materials with high anisotropy. The contribution of an individual to the expansion of the Bragg reflection line [32] is expressed as:

$$\beta_{hkl} = \beta_s + \beta_D. \qquad (7)$$

This expression represents the width caused by size strain. In correspondence to the FWHM of a peak, the strain remains uniform along the crystallographic direction in the W–H relationship.

Equations (8) and (9) are referred to as the W–H equation, which represents the UDM. According to this model, crystals should be isotropic because the strain should be constant in all crystallographic orientations. A plot with 4sinθ values along the x-axis and $\beta\cos\theta$ values along the y-axis was generated for each detected diffraction peak. The lattice strain ε is given by the slope of the linear fit, whereas the crystallite size D is represented by the plot's y-intercept [33]. The crystallite size and strain are determined as the slope of the fitted line, as shown in Figure 3. The sizes of nanoparticles are shown in Table 2.

Strain is referred by employing a generalized Hooke's law in the USDM, which maintains a simple linear proportionality between the stress and strain, as provided by $\sigma = E\varepsilon$, where E is Young's modulus, or the modulus of elasticity, and σ is the crystal stress. This equation only applies to modest strain and is only an approximation.

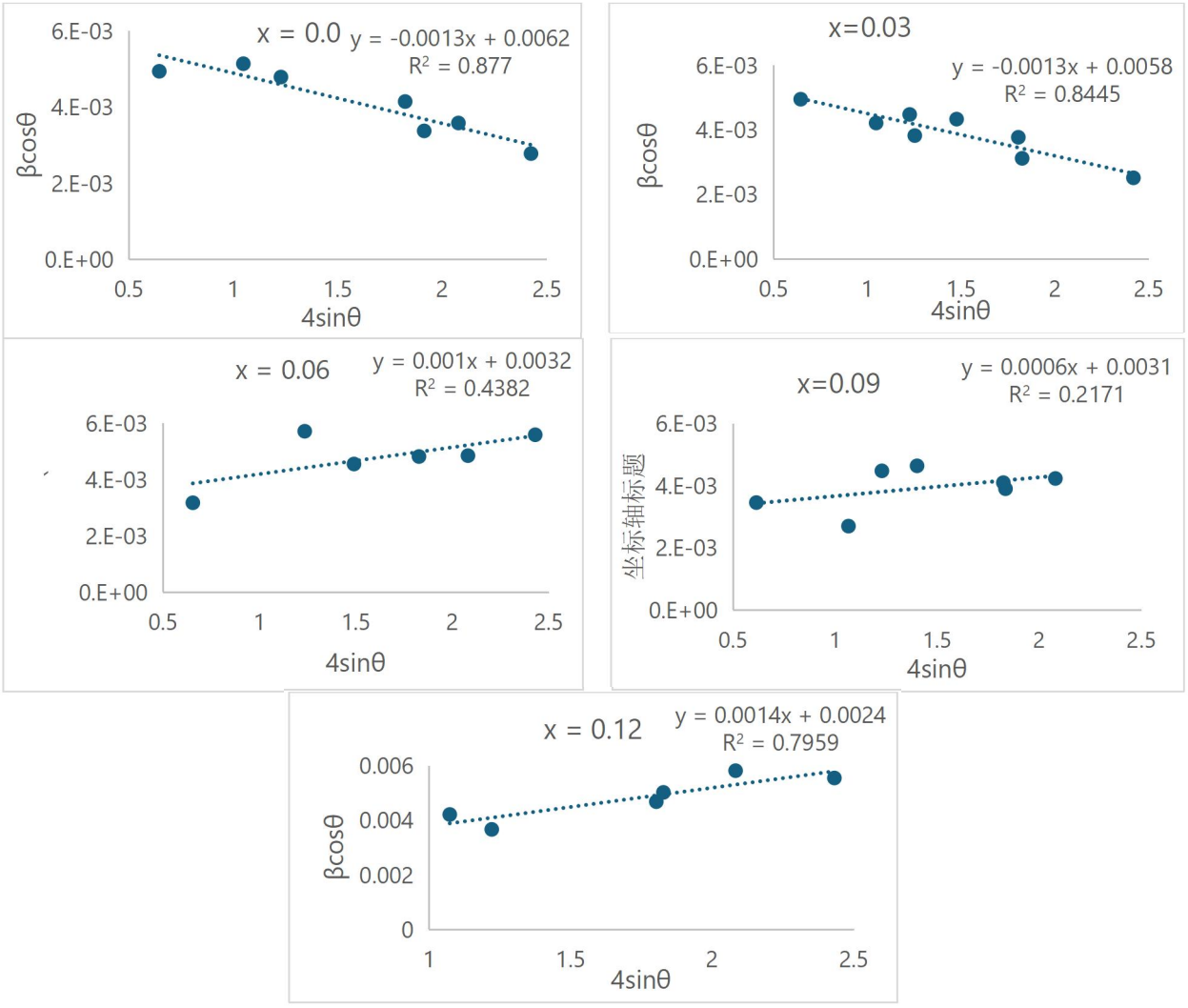

Figure 3. UDM analysis of $Co_xCu_{0.2}Zn_{0.8-x}Fe_2O_4$ nanoferrites.

Using Hooke's law approximation of the equation yields the equation which represents a Uniform stress model (USDM) [34].

$$\beta\cos\theta = \frac{K\lambda}{D} + \frac{4sin\sigma\theta}{E_{hkl}}, \qquad (8)$$

where σ is the stress, and E_{hkl} is the elastic modulus for the crystal direction. Plotting $\beta\cos\theta$ versus $4\sin\theta/E_{hkl}$ yields cut-off value = $(K\lambda)/D$ and slope = σ. This model has the advantage of integrating mechanical properties into microscopic analysis.

Stress can be inferred from the slope of the line drawn between $4\sin\theta/E_{hkl}$ and $\beta\cos\theta$. Young's modulus can be calculated through the relation [35].

$$\frac{1}{E} = S_{11} - (2S_{11} - 2S_{12} - S_{44})\frac{k^2l^2+l^2h^2+h^2k^2}{(h^2+k^2+l^2)}. \qquad (9)$$

The elastic compatibilities for Fe_3O_4 are S_{11}, S_{12}, and S_{44} and are represented by:

$$S_{11} = \frac{(c_{11}+c_{12})}{(c_{11}-c_{12})(c_{11}+2c_{12})},$$

$$S_{12} = \frac{(-2c_{12})}{(c_{11}-c_{12})(c_{11}+2c_{12})},$$

$$S_{44} = \frac{1}{c_{44}}.$$

The elastic constant values c_{11}, c_{12}, and c_{44}, are 272, 158, and 96 GPa, respectively [36]. The USDM plots are displayed in Figure 4, and the results are shown in Table 2.

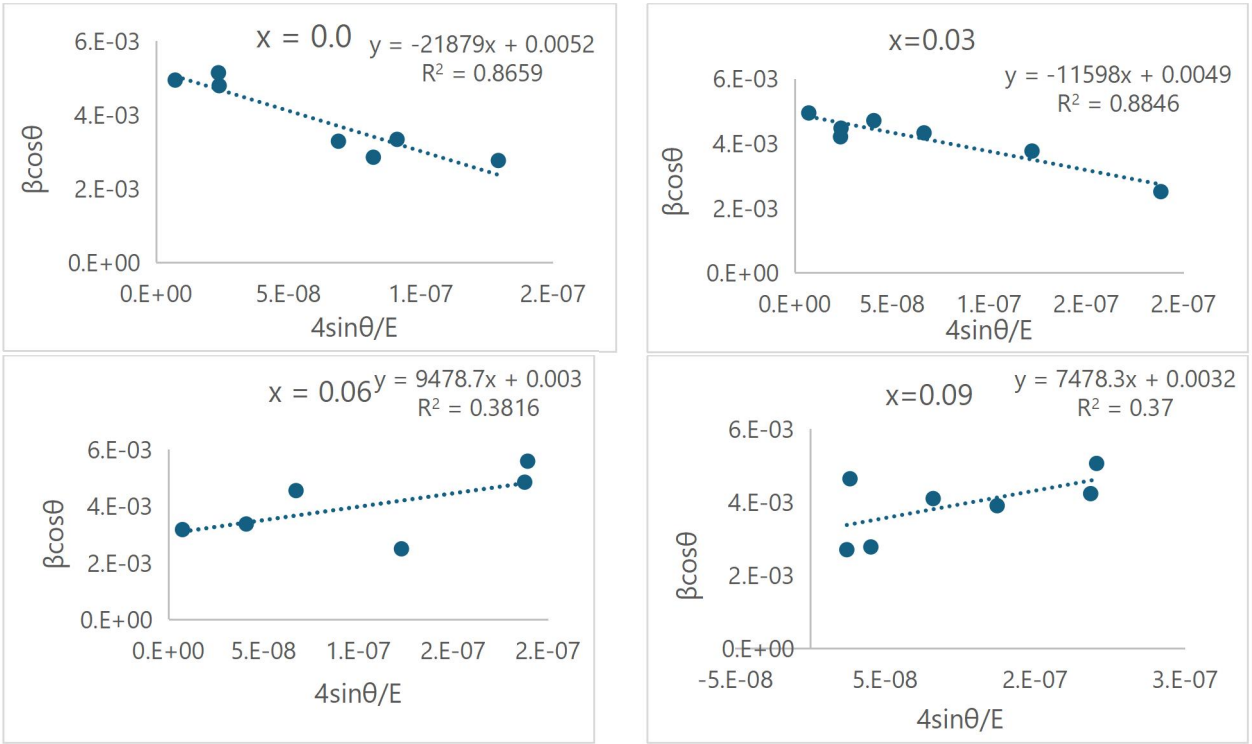

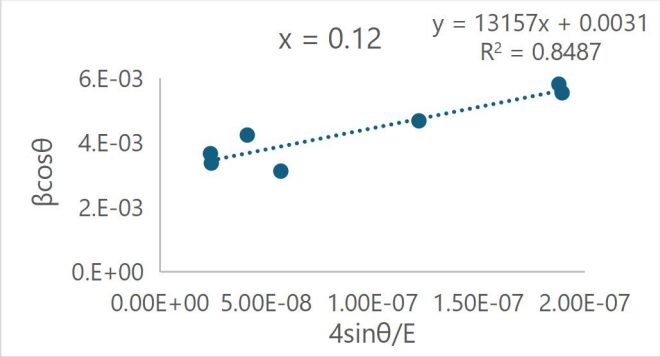

Figure 4. USDM analysis of $Co_xCu_{0.2}Zn_{0.8-x}Fe_2O_4$ nanoferrites.

The UDEDM is another variant of the W–H model that is employed to analyze the lattice energy density of crystals. It is applicable under the conditions of continuous proportionality in homogeneity. It is a further development of the W–H method, taking into account the relationship between stresses and deformation energy density within the crystal. This model assumes that the elastic energy density U is uniformly distributed and is calculated by using the equation [37]:

$$U = \frac{\sigma^2}{2E_{hkl}}. \qquad (10)$$

By using $\sigma = \varepsilon E_{hkl}$, the W–H equation can be reformulated as [38]:

$$\beta_{hkl}\cos = \frac{K\lambda}{D} + (4\sin\theta\,[\frac{2U}{E}]^{\frac{1}{2}}), \qquad (11)$$

where U is the deformation energy density, and E_{hkl} is the elastic modulus for the crystal direction. By plotting $\beta_{hkl}\cos\theta$ versus $\sin\theta$, the crystal volume D can be obtained from the cut section, whereas the slope provides a value related to the root of the elastic energy density of the material.

For an elastic system, Hooke's law, in terms of strain, can be expressed as follows:

The relationship (12) enables the calculation of the lattice stress, strain, and energy density by using the graph of $4\sin\theta\ (2/E)^{1/2}$ against $\beta\cos\theta$, as illustrated in Figure 5. The related findings are presented in Table 2.

The analysis of XRD results using the Scherer and W–H models reveals crucial information about the structural properties of $Co_xCu_{0.2}Zn_{0.8-x}Fe_2O_4$ nanoferrites. The data show that crystallite size and internal stresses change systematically with increasing cobalt content, reflecting the complex effect of ionic substitution on the microstructure of the material.

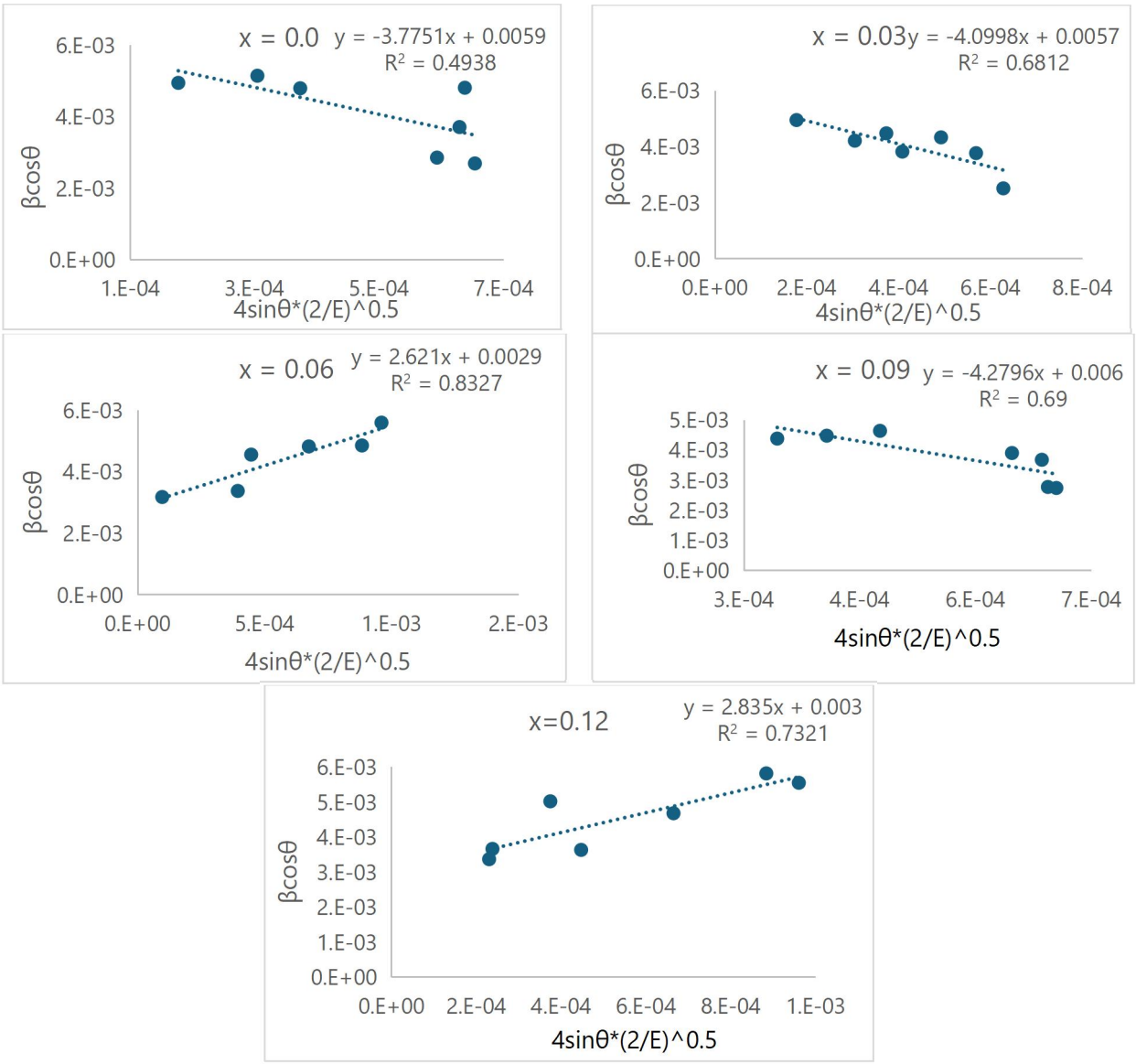

Figure 5. UDEDM analysis of $Co_xCu_{0.2}Zn_{0.8-x}Fe_2O_4$ nanoferrites.

Table 2. Microstructural parameters of $Co_xCu_{0.2}Zn_{0.8-x}Fe_2O_4$ nanoferrites.

x	Scherrer method- D_{Sch} (nm)	W–H method								
		UDM		USDM			UDEDM			
		D (nm)	ε $\times 10^{-3}$	D (nm)	ε × 10^{-4}	σ × 10^4 (pa)	D (nm)	ε × 10^{-3}	σ × 10^4 (pa)	U ($J \cdot m^{-3}$)
0.00	35.4	22.4	−1.3	26.7	−7.4	2.2	23.5	−1.14	2.5	14.3
0.03	35.1	23.9	−1.3	27.2	−5.3	1.2	24.3	−1.24	2.7	16.8
0.06	31.6	43.3	1	46.2	4.9	0.95	47.8	0.85	1.6	6.9
0.09	36.3	44.7	0.6	43.3	3.7	0.75	23.1	−1.3	2.8	18.3
0.12	31.8	57.7	1.4	44.7	6.5	1.3	46.2	0.89	1.8	8.04

The Scherrer technique and three versions of the W–H method, namely, UDM, USDM, and UDEM, were used to examine the effect of different cobalt concentrations on the microstructural characteristics of $Co_xCu_{0.2}Zn_{0.8-x}Fe_2O_4$ nanoferrites. The findings demonstrate good sensitivity to chemical composition and

notable heterogeneity between different techniques [39]. The crystallographic size calculated by the Scherrer method is between 31.6 and 36.3 nm and has not obviously increased. The lowest value (31.6 nm) and maximum value (36.3 nm) are observed at x = 0.06 and x = 0.09, respectively. This result indicates that that while partial zinc substitution at these ratios can have an effect on crystallinity, the crystallographic size does not markedly change.

However, the W–H models provide markedly increased crystal size values because while the Scherrer technique assumes that peak width is caused only by small particle size, they account for the effect of strain and stress on the amplitude of diffraction peaks [40].

Grain size increases from 22.4 nm at x = 0 to 57.7 nm at x = 0.12, indicating that among models, the UDM produces the highest values as x increases. This increase results from this model's full disregard of the effect of stress, with the model merely taking strain into account without distinguishing between various causes [41]. The USDM, which accounts for uniform stress, produces intermediate values between 26.7 and 46.2 nm and yields consistent changes in x, where stress σ gradually decreases from 2.2×10^4 Pa at x = 0 to 0.75×10^4 Pa at x = 0.09 before slightly increasing to 1.3×10^4 Pa at x = 0.12. The decline at x = 0.09 can be explained by an increase in structure and the relaxation of internal stresses that may be induced by the size conformity of the input ions [42]. The UDEM revealed unusual behavior, in which the crystal volume increases to 47.8 nm at x = 0.06 then suddenly decreases to 23.1 nm at x = 0.09 before increasing again to 46.2 nm at x = 0.12. The model's peak strain energy U (18.3 J/m^3), strain ε (1.3×10^{-3}), and stress σ (2.8×10^4 Pa) all coincide with the abrupt decline at x = 0.09. This behavior suggests that the relationship between strain energy and volume is not linear but rather depends on the stress distribution inside the crystal lattice because the x = 0.09 configuration induces large internal strain despite the modest crystal volume [43].

Analyzing the strain between models reveals that the ε values of the UDM range from 0.6 to 1.4 and are in the order of 10^{-3}, whereas those of the USDM are 10-fold smaller and are in the order of 10^{-4}, signaling the model's sensitivity to physical assumptions. Analogous results have been reported by previous investigations on zinc and manganese nanoferrites using the size–strain diagram and W–H analysis [44]. Overall, this result indicates that x = 0.06 and x = 0.12 yield large crystalline volumes, albeit with low strain energies (6.9 and 8.04 J/m^3 in this case), which may be suitable when a homogeneous structure is desired. At x = 0.09, however, a noticeable difference exists among the models: the UDEM displays the lowest volume and maximum strain energies, whereas the Scherrer technique and USDM provide average volumes and low strain. This disparity implies that despite being thorough, the UDEM may be sensitive to slight changes in strain distribution because of its reliance on strain energy density [45].

The change in the crystal lattice parameters can be explained as follows: with the substitution of cobalt, the ionic radius and cation distribution within the spinel structure change. Although the radii of Zn^{2+} and Co^{2+} are similar, their different bond properties and preferred positions lead to lattice distortion. Zn^{2+} preferentially occupies A sites, whereas Co^{2+} tends to occupy B sites, resulting in cation redistribution. This new distribution leads to local distortion in the crystal lattice and contributes to internal stress, which is reflected in the nonlinear change in microstructure parameters. Partial stress relaxation may

occur at certain structures because of improved ionic stacking and further crystal structure reorganization [46]

Furthermore, the difference between the crystal sizes derived from the Scherrer and W–H methods arise from the fact that the Scherrer equation only considers the expansion due to volume, whereas the W–H method takes into account the effects of volume and stress. This situation results in a realistic estimate of crystal size and explains the methodological divergence between the two methods [47].

Field-emission scanning electron microscopy (FESEM) images (Fig. 7) show the surface morphology of the prepared nanoferrites. ImageJ software was used for particle size analysis. All visible particles in each FESEM image for each sample were selected to ensure the accuracy of statistical results. Particle size distribution, mean particle size, and standard deviation were then calculated. Nanoparticles are formed with a heterogeneous size and shape distribution, appearing spherical. This morphological diversity is presumed to be due to variations in the growth mechanism during colloidal solution preparation, where the cobalt ratio determines crystallization kinetics [48].

The FESEM images also show good crystallinity of the nanoparticles, revealing clear granular boundaries in most areas. This finding is consistent with XRD results, which indicate the presence of a regular, impurity-free cubic crystalline phase. The addition of cobalt appears to affect particle size and shape, with minimal agglomeration observed in samples with high cobalt content. This phenomenon is attributed to the influence of cobalt ions on crystallization kinetics and particle growth during solidification and thermal decomposition [49].

At x = 0.0, the average grain size is approximately 74 ± 8 nm, and cobalt substitution and remarkable grain growth are not observed. As the cobalt content increases to x = 0.03, the average grain size decreases to 68 ± 6 nm, suggesting that cobalt addition inhibits grain growth because of the presence of Co^{2+} in the crystal lattice. At x = 0.06, the average grain size reaches 83 ± 10 nm, which is larger than that observed in the previous two samples. These results indicate a rearrangement in the crystal structure and suggest that the influences of the ionic radii of Co^{2+} and Zn^{2+} on agglomeration facilitation differ. However, when x = 0.09, the particle size decreases again to 65 ± 5 nm, which is the smallest size in all samples, demonstrating the effect of partial cobalt substitution on reducing particle size and preventing agglomeration [50].

At the highest concentration (x = 0.12), the average particle size increases again by 75 ± 9 nm, indicating that exceeding a certain cobalt content may promote particle growth by initiating agglomeration and increasing intercrystalline attraction. These observations demonstrate that substituting Zn^{2+} for Co^{2+} alters particle size [51].

A clear difference can be observed between the crystal size extracted from XRD and the particle size estimated from FESEM images. The crystal size, which ranges from 22 nm to 58 nm, reflects the size of the coherent diffraction bands, whereas the large particle size (65 ± 5 nm to 83 ± 10 nm) corresponds to agglomerated grains. This difference indicates that each particle is composed of multiple crystals, confirming the polycrystalline nature of the samples. Furthermore, the increase in particle size can be attributed to agglomeration resulting from grain growth during calcination. This phenomenon is a common behavior in nanoferrite systems and reflects the merging of small crystals to form large particles [52].

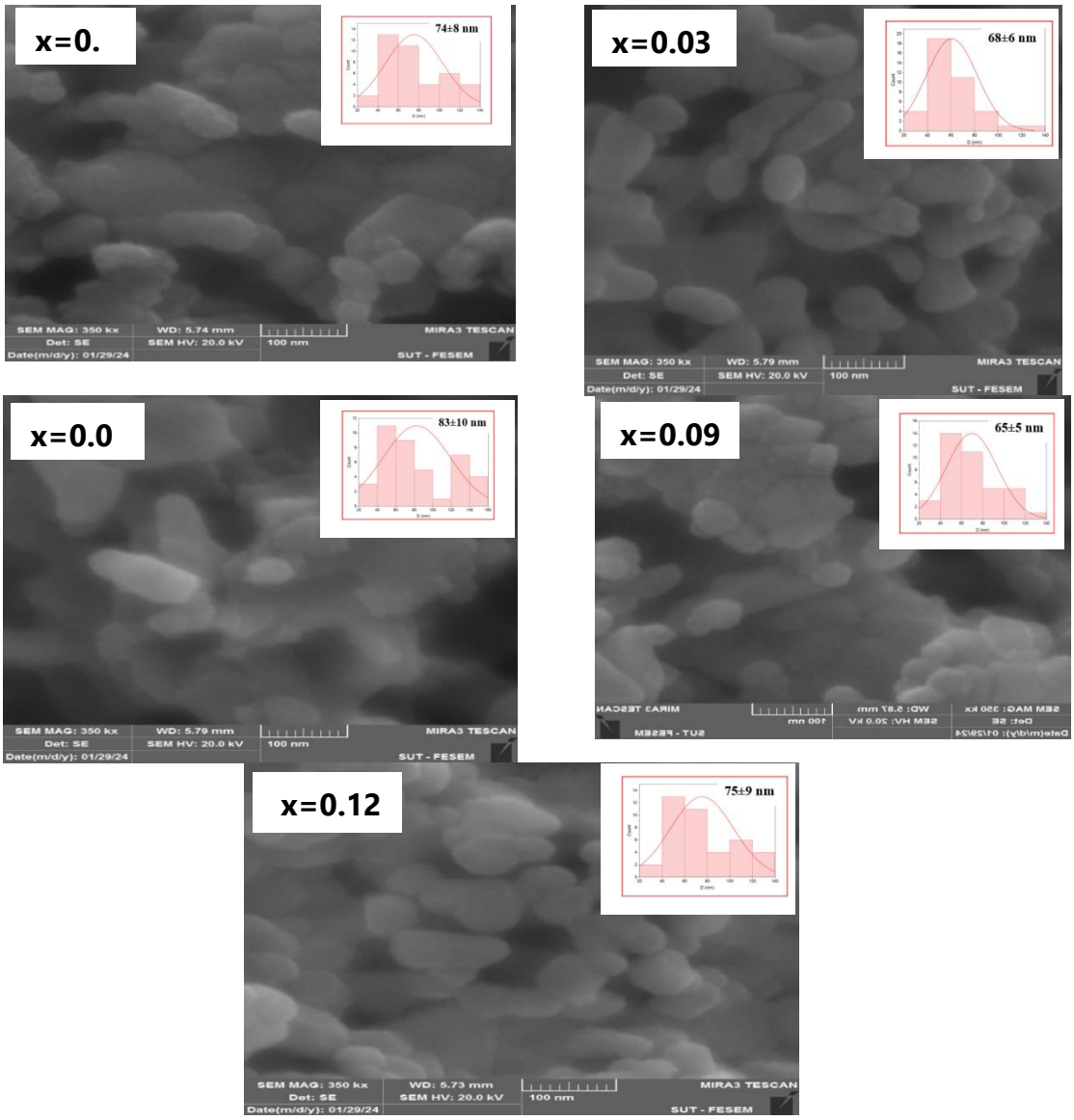

Figure 7. FESEM images and grain distribution of $Co_xCu_{0.2}Zn_{0.8-x}Fe_2O_4$ nanoferrites.

4. Conclusion

$Co_xCu_{0.2}Zn_{0.8-x}Fe_2O_4$ nanoferrites were prepared through the sol–gel route, and the effects of cobalt ion substitution on their microstructural and microscopic properties were investigated. XRD results confirmed the formation of a cubic spinel phase for all models, with a change in the lattice constant due to cation substitution.

W–H models (UDM, USDM, and UDEDM) demonstrated that variations in crystallite size, strain, and stress values depended on model assumptions, highlighting the importance of using multiple models for an accurate understanding of microstructures. The results also indicated that cobalt ion substitution leads to nonlinear changes in internal stress and strain energy.

FESEM images revealed spherical-to-semispherical nanoparticles with agglomeration and particle sizes ranging from 65 ± 5 nm to 83 ± 10 nm. The difference between the crystallite sizes inferred from XRD and the grain sizes inferred from FESEM also confirmed the polycrystalline nature of the prepared

samples. Overall, the results of this work indicate that cobalt ion substitution directly affects the structural and microscopic properties of the prepared compounds.

Availability of Data and Materials: The datasets used and analyzed during the current study are available from the corresponding author on reasonable request.

Author Contributions: All authors contributed to the study conception and design, material preparation, data collection and analysis, and manuscript writing. All authors have read and approved the final manuscript. All authors contributed to editorial changes in the manuscript. All authors have participated sufficiently in the work and agreed to be accountable for all aspects of the work.

Funding: This research received no external funding.

Conflict of Interest: The authors declare that they have no known competing financial interests or personal relationships that could have appeared to influence the work reported in this paper.

References

1. Vedrtnam, A.; Kalauni, K.; Dubey, S.; Kumar, A. A comprehensive study on structure, properties, synthesis and characterization of ferrites. *AIMS Materials Science* 2020, 7(6), 800–835. https://doi.org/10.3934/matersci.2020.6.800.
2. Javed, F.; Abbas, M.A.; Asad, M.I.; Ahmed, N.; Naseer, N.; Saleem, H.; Ahmad, N.M. Gd^{3+} doped $CoFe_2O_4$ nanoparticles for targeted drug delivery and magnetic resonance imaging. *Magnetochemistry* 2021, 7(4), 47. https://doi.org/10.3390/magnetochemistry7040047.
3. Hossain, M.D.; Jamil, A.T.M.K.; Hasan, M.R.; Ali, M.A.; Esha, I.N.; Hossain, M.S.; Khan, M.N.I. Impact of V substitution on the physical properties of Ni–Zn–Co ferrites: structural, magnetic, dielectric and electrical properties. *Materials Research Express* 2021, 8(4), 046102. https://doi.org/10.1088/2053-1591/abf3c9.
4. Wiegmann, T.; et al. Operando identification of the reversible skin layer on Co_3O_4 as a three-dimensional reaction zone for oxygen evolution. *ACS Catalysis* 2022, 12(6), 3256–3268. https://doi.org/10.1021/acscatal.1c05169
5. Niederberger, M. Nonaqueous sol–gel routes to metal oxide nanoparticles. *Accounts of Chemical Research* 2007, 40(9), 793–800. https://doi.org/10.1021/ar600035e.
6. Din, I.U.; et al. Study of annealing conditions on particle size of nickel ferrite nanoparticles synthesized by wet chemical route. *Synthesis and Reactivity in Inorganic, Metal-Organic, and Nano-Metal Chemistry* 2015, 46(3), 405–408. https://doi.org/10.1080/15533174.2014.988226
7. Soria, G.D.; Serrano, A.; Prieto, J.E.; Quesada, A.; Gorni, G.; de la Figuera, J.; Marco, J.F. Effect of annealing in the formation of well-crystallized and textured $SrFe_{12}O_{19}$ films grown by RF magnetron sputtering. *Journal of Materials Research* 2023, 38(4), 1119–1128. https://doi.org/10.1557/s43578-022-00822-9
8. Jannat, M.R.; Biswas, B.; Rahman, M.L.; Ahmed, M.F.; Hossain, M.J.; Khanam, J.; Sharmin, N. Validity of crystallite size determination methods based on XRD peak broadening in pure and metal-doped nickel ferrites. *Results in Materials* 2025, 28, 100762. https://doi.org/10.1016/j.rinma.2025.100762
9. Rajeswari, P.; Dhanuskodi, S. Microstructural effects of Mn^{2+} ions in ZnO nanoparticles. *Crystal Research and Technology* 2013, 48(9), 589–598. https://doi.org/10.1002/crat.201300102.
10. Edrees, S.J.; Kareem, S.J.; Fadel, A.M. Morphological characterizations of spinel nanoparticles synthesized by sol-gel method. *Journal of Physics: Conference Series* 2021, 1973(1), 012132. https://doi.org/10.1088/1742-6596/1973/1/012132
11. Hamid, R.K.A.E.; El-Sayed, O.; Ghozza, M.H. Structural, fluorescence and magnetic properties of Cr^{3+} cation substituted of $Co_{0.7}Mn_{0.3}Cr_xFe_{2-x}O_4$ ($0 \leq x \leq 1$) nanoparticles. *Applied Physics A* 2025, 131(5). https://doi.org/10.1007/s00339-025-08414-0
12. Mahdi, H.I.; Watan, A.W.; Al-Saadi, T.M. Fabrication of NH_3 gas sensors using lithium-substituted $ZnFe_2O_4$ nano-ferrite. *Bulletin of Materials Science* 2025, 48(3), 89. https://ssrn.com/abstract=4921017
13. Mohammed, A.J.; Hamdan, S.A. The Influence of the Various pH Value on Structural and Magnetic Properties of Cobalt Ferrite Nanostructure. *Mustansiriyah Journal of Pure and Applied Sciences* 2024, 2(1), 15–30. https://doi.org/10.47831/mjpas.v2i1.97
14. Al-Tabbakh, A.A.; et al. Crystallite size and lattice strain of lithiated spinel material for rechargeable battery by x-ray diffraction peak-broadening analysis. *International Journal of Energy Research* 2019, 43(5), 1903–1911. https://doi.org/10.1002/er.4390

15. Carta, D.; et al. A structural and magnetic investigation of the inversion degree in ferrite nanocrystals MFe_2O_4 (M = Mn, Co, Ni). *Journal of Physical Chemistry C* 2009, 113(20), 8606–8615. https://doi.org/10.1021/jp901077c
16. Rida, A.; Rouhaud, E.; Makke, A.; Micoulaut, M.; Mantisi, B. Study of the effects of grain size on the mechanical properties of nanocrystalline copper using molecular dynamics simulation with initial realistic samples. *Philosophical Magazine* 2017, 97(27), 2387–2405. https://doi.org/10.1080/14786435.2017.1334136
17. Saheb, L.; Al-Saadi, T.M. Study of ($Zn_{0.7}$ $Mn_{0.3-x}$ $Ag_{0.3}$ Fe_2O_4) ferrite nanoparticles synthesized by auto combustion method for NO_2 gas sensing. *AIP Conference Proceedings* 2023, 2591(1), 040011. https://doi.org/10.1063/5.0120309
18. Guragain, D.; Rai, B.K.; Yoon, S.; Poudel, T.P.; Bhandari, S.C.; Mishra, S.R. Effect of terbium ion substitution in inverse spinel nickel ferrite: structural and magnetic study. *Magnetochemistry* 2020, 6(1), 14. https://doi.org/10.3390/magnetochemistry6010014
19. Hall, D.S.; et al. Nickel hydroxides and related materials: A review of their structures, synthesis and properties. *Proceedings of the Royal Society A* 2015, 471(2174), 20140792. https://doi.org/10.1098/rspa.2014.0792
20. Vinnik, D.A.; Sherstyuk, D.P.; Zhivulin, V.E.; Zhivulin, D.E.; Starikov, A.Y.; Gudkova, S.A.; ...; Trukhanov, A.V. Impact of the Zn–Co content on structural and magnetic characteristics of the Ni spinel ferrites. *Ceramics International* 2022, 48(13), 18124–18133. https://doi.org/10.1016/j.ceramint.2022.03.070
21. Bober, D.B.; Kumar, M.; Rupert, T.J. Nanocrystalline grain boundary engineering: Increasing Σ3 boundary fraction in pure Ni with thermomechanical treatments. *Acta Materialia* 2015, 86, 43–54. https://doi.org/10.1016/j.actamat.2014.11.034
22. Deringer, V.L.; et al. Gaussian process regression for materials and molecules. *Chemical Reviews* 2021, 121(16), 10073–10141. https://doi.org/10.1021/acs.chemrev.1c00022
23. Goloveshkin, A.S.; et al. Probing hydrogen-bonding properties of a negatively charged MoS_2 monolayer by powder X-ray diffraction and density functional theory calculations. ACS Omega 2020, 5(9), 4603–4610. https://doi.org/10.1021/acsomega.9b04161
24. Atif, M.; Rafique, T.; Rehman, A.U.; Wahab, H.; Khalid, W.; Ali, Z.; Nadeem, M. Effect of cation distribution on the structural and dielectric properties of $Ni_{0.5-x}Co_xZn_{0.5}Fe_2O_4$ ($0.0 \leq x \leq 0.5$) ferrites. *Journal of Materials Science: Materials in Electronics* 2020, 31(14), 10970–10980. https://doi.org/10.1007/s10854-020-03645-8
25. Khomskii, D.I.; Streltsov, S.V. Magnetic oxides. In *Encyclopedia of Condensed Matter Physics*, 2nd ed.; 2024; Volume 2, pp. 98–111. https://doi.org/10.48550/arXiv.2212.14176
26. Muslim, T.; Kadhim, S.A. The Gas Sensitivity Properties of Nano Ferrite $Cu_xAl_{0.3-x}Ni_{0.7}Fe_2O_4$ Synthesized by Sol-Gel Method. *Ibn AL-Haitham Journal For Pure and Applied Sciences* 2023, 36(4), 159–170. https://doi.org/10.30526/36.4.3118
27. Yuvaraj, S.; Ramachandran, S.; Sheela, R.; Jothiramalingam, R.; Isaac, R.S.R.; Sundararajan, M.; Sasikumar, S. Synthesis and optical and magnetic property characterization of $Zn_{1-x-y}Co_xNiyFe_2O_4$ (x & y= 0, 0.05, 0.15 and 0.25) nanoparticles. *Journal of Ovonic Research* 2025, 21(3), 279–284. https://doi.org/10.15251/JOR.2025.213.279
28. Scardi, P. Diffraction line profiles in the Rietveld method. *Crystal Growth & Design* 2020, 20(10), 6903–6916. https://doi.org/10.1021/acs.cgd.0c00956
29. Abed, A.H.; Khodair, Z.T.; Al-Saadi, T.M.; Al-Dhahir, T.A. Study the evaluation of Williamson–Hall (WH) strain distribution in silver nanoparticles prepared by sol-gel method. *AIP Conference Proceedings* 2019, 2123(1), 020019. https://doi.org/10.1063/1.5116946
30. Mahdi, H.I.; Al-Saadi, T.M.; Bakr, N.A. Fabrication and characterization of $Co_xMn_{0.25-x}Mg_{0.75}Fe_2O_4$ nanoparticles for H_2S sensing applications. *Journal of Materials Science: Materials in Electronics* 2023, 34(22), 1634. https://doi.org/10.1007/s10854-023-11064-8
31. Mohapatra, R.; Kaundal, J.B.; Goswami, Y.C. Synthesis of optically important transparent SnS_2/PS composites films through chemical route and their photocatalytic applications. *Journal of Ovonic Research* 2022, 18(3), 343–355. https://doi.org/10.15251/JOR.2022.183.343
32. Al-Saadi, T.M. Investigating the structural and magnetic properties of nickel oxide nanoparticles prepared by precipitation method. *Ibn Al-Haitham Journal For Pure and Applied Sciences* 2022, 35(4), 94–103. https://doi.org/10.30526/35.4.2872.
33. Mote, V.D.; Purushotham, Y.P.; Dole, B.N. Williamson-Hall analysis in estimation of lattice strain in nanometer-sized ZnO particles. *Journal of Theoretical and Applied Physics* 2012, 6(1), 6. https://doi.org/10.1186/2251-7235-6-6
34. Nath, D.; Singh, F.; Das, R. X-ray diffraction analysis by Williamson-Hall, Halder-Wagner and size-strain plot methods of CdSe nanoparticles-a comparative study. *Materials Chemistry and Physics* 2020, 239, 122021. https://doi.org/10.1016/j.matchemphys.2019.122021

35. Knowles, K.M. The plane strain Young's modulus in cubic materials. *Journal of Elasticity* 2017, 128(2), 147–173. https://doi.org/10.1007/s10659-017-9621-x
36. Al-Saadi, T.M.; Kamil, Z.A. Study the Effect of Manganese Ion Doping on the Size-Strain of SnO_2 nanoparticles Using X-Ray Diffraction Data. *Ibn AL-Haitham Journal for Pure and Applied Sciences* 2023, 36(3), 158–166. https://doi.org/10.30526/36.3.3052
37. Prabhu, Y.T.; Rao, K.V.; Kumar, V.S.S.; Kumari, B.S. X-ray analysis by Williamson-Hall and size-strain plot methods of ZnO nanoparticles with fuel variation. *World Journal of Nano Science and Engineering* 2014, 4(1). https://doi.org/10.4236/wjnse.2014.41004
38. Devesa, S.; Rooney, A.P.; Graça, M.P.; Cooper, D.; Costa, L.C. Williamson-Hall analysis in estimation of crystallite size and lattice strain in $Bi_{1.34}Fe_{0.66}Nb_{1.34}O_{6.35}$ prepared by the sol-gel method. *Materials Science and Engineering: B* 2021, 263, 114830. https://doi.org/10.1016/j.mseb.2020.114830
39. Mote, V.D.; Purushotham, Y.P.; Dole, B.N. Williamson-Hall analysis in estimation of lattice strain in nanometer-sized ZnO particles. *Journal of Theoretical and Applied Physics* 2012, 6(1), 6. https://doi.org/10.1186/2251-7235-6-6
40. Augustin, M.; Balu, T. Estimation of Lattice Stress and Strain in Zinc and Manganese Ferrite Nanoparticles by Williamson–Hall and Size-Strain Plot Methods. *International Journal of Nanoscience* 2017, 16(3), 1650035. https://doi.org/10.1142/S0219581X16500356
41. Kolekar, R.Y.; Kapatkar, S.B.; Mathad, S.N. Synthesis and Characterization of $Co_{0.8-x}$ Ni_x $Zn_{0.2}$ Fe_2O_4 Ferrites by Williamson–Hall and Size–Strain Plot Methods. *Acta Chemica Iasi* 2019, 27, 73–86. https://doi.org/10.2478/achi-2019-0006
42. Varaprasad, B.B.V.S.; Ramesh, K.V.; Srinivas, A. Structural, morphological and magnetic properties of divalent copper-substituted Co–Zn Nanoferrites. *International Journal of Modern Physics B* 2018, 32(14), 1850172. https://doi.org/10.1142/S0217979218501722
43. Madansure, Y.S.; Gurav, S.K.; Balsure, S.D.; Gaikwad, P.K.; Imran, A.; El-Toni, A.M.; ...; Kadam, R.H. X-ray diffraction analysis by Williamson-Hall, strain-size, Halder-Wagner, and Nelson–Riley methods, and its co-relationship with elastic and magnetic properties of Ce^{3+} substituted Fe-rich cobalt ferrite. *Journal of Materials Science: Materials in Electronics* 2026, 37(10), 706. https://doi.org/10.1007/s10854-026-17126-x
44. Augustin, M.; Balu, T. Estimation of Lattice Stress and Strain in Zinc and Manganese Ferrite Nanoparticles by Williamson–Hall and Size-Strain Plot Methods. *International Journal of Nanoscience* 2017, 16(03), 1650035. https://doi.org/10.1142/S0219581X16500356
45. Abed, A.H.; Mahan, N.K.; Abdulrahman, H.S.; Al-Saadi, T.M. Investigating the Effect of Cobalt Ions on the Optical and Structural Properties of Zinc Ferrite Synthesized by the Sol-Gel Technique. *Journal of Ovonic Research* 2026, 22(1), 119–130. https://doi.org/10.15251/JOR.2026.221.119
46. Feng, B.C.; Tegus, O.; Ochirkhyag, T.; Odkhuu, D.; Tsogbadrakh, N.; Sangaa, D.; Davaasambuu, J. Study of structural and magnetic properties of Spinel Zn doped cobalt ferrites. *Solid State Phenomena* 2020, 310, 124–133. https://doi.org/10.4028/www.scientific.net/SSP.310.124
47. Jabir, S.A.A.; Harbbi, K.H. A comparative study of Williamson-Hall method and size-strain method through X-ray diffraction pattern of cadmium oxide nanoparticle. *AIP Conference Proceedings* 2020, 2307(1), 020015. https://doi.org/10.1063/5.0033762
48. Pan, L.; Cao, D.; Jing, P.; Wang, J.; Liu, Q. A novel method to fabricate $CoFe_2O_4/SrFe_{12}O_{19}$ composite ferrite nanofibers with enhanced exchange coupling effect. *Nanoscale Research Letters* 2015, 10(1), 131. https://doi.org/10.1186/s11671-015-0829-z
49. Khusnuriyalova, A.F.; et al. Preparation of cobalt nanoparticles. *European Journal of Inorganic Chemistry* 2021, 2021(30), 3023–3047. https://doi.org/10.1002/ejic.202100367
50. Sinko, K.; Manek, E.; et al. Liquid-phase syntheses of cobalt ferrite nanoparticles. *Journal of Nanoparticle Research* 2012, 14, 894. https://doi.org/10.1007/s11051-012-0894-5
51. Rizvi, M.; Gerengi, H.; Gupta, P. Functionalization of nanomaterials: Synthesis and characterization. *ACS Symposium Series* 2022, 1–26. https://doi.org/10.1021/bk-2022-1418.ch001

52. Mataev, M.; Madiyarova, A.; Abdraimova, M.; Tursyn, Z.; Ramachandran, K. Structure Property–Application Relationships of Spinel Ferrite Nanoparticles: From Synthesis to Functional Systems. *International Journal of Molecular Sciences* 2026, 27(5), 2096. https://doi.org/10.3390/ijms27052096